Astron. Astrophys. 319, 166–175 (1997)

ASTRONOMY
AND
ASTROPHYSICS

Irradiated red giant atmospheres in S-type symbiotic stars

M. Schwank, W. Schmutz, and H. Nussbaumer

Institute of Astronomy, ETH-Zentrum, CH-8092 Zürich, Switzerland

Received 15 May 1996 / Accepted 17 July 1996

Abstract. We present non-LTE calculations for an expanding red giant's atmosphere ionized from the outside by the radiation of a nearby hot radiation source. We show that the hydrogen emission lines emerge from a narrow transition zone where hydrogen changes from ionized to neutral. In this region the Balmer lines are optically thick, and their profiles crucially depend on the magnitude of optical thickness which in turn, depends on the velocity gradient within that region. Balmer decrements of the model calculations depend on the densities in the recombination zone of the radiatively ionized wind. We find a large variety of complex line profiles, that in some cases could be mistaken for accretion disk profiles. The profiles depend on the velocity law in the formation zone at sub-sonic velocities, but contrary to expectation, the profiles do not reflect the terminal velocity of the wind. The central part of our model profiles compare well with the observed profile of the eclipsing binary SY Mus at maximum light.

Key words: radiative transfer – methods: numerical – binaries: symbiotic – stars: novae – stars: SY Mus

1. Introduction

The generally accepted model presents symbiotic systems as low mass binaries in a late evolutionary stage. Infrared observations suggest a partition into S-type and D-type symbiotics. The IR flux of S-types agrees with the spectral distribution expected from a cool star, whereas the D-types show the presence of still cooler dust. It turns out that the two classes correspond to significant differences in the binary separation. S-type symbiotics are binaries with separations of a few AU, whereas D-types are much wider. The S-type symbiotics therefore allow a closer interaction between the two stars, they are the subject of this investigation.

In S-type systems the two stellar components are a hot white dwarf of typically $R_* \approx 0.1 R_\odot$ and $T_* \approx 100\,000$K, and a late type giant, typically M III. (In D-type symbiotics the cool star is mostly a Mira type.) Symbiotic systems also show nebular emission lines. Determinations of nebular abundances yield values which fit those of red giants (Nussbaumer et al. 1988). We may therefore assume that the nebula is fed by mass loss of the red giant. Even the closest symbiotic system has a distance of 200 pc. With binary separations of 10 AU or less we cannot, at present, spatially resolve the two stellar components, and even less can we resolve the nebular structure within their orbits. However, access can be obtained by closely studying line profiles in combination with eclipse effects.

Line profiles of symbiotic stars show in many cases a rich structure consisting of several components, and the components change with phase. Extended sets of observations from northern and southern symbiotics are given in Ivison et al. (1994) and van Winkel et al. (1993). Eclipse observations show that the nebular emission can originate very close to the red giant. This is certainly the case for RW Hya (Schild et al. 1996), and for SY Mus (Schmutz et al. 1994). Other observations and considerations have led to a similar conclusion in other objects, e.g. V443 Her (Dobrzycka et al. 1993), or AG Peg (Kenyon et al. 1993). The question then arises, how much of the structure in an emission line is due to a peculiar structure of the nebula, and how much to illumination effects in the outermost part of the stellar atmosphere. Proga et al. (1996) study this problem based on a plane-parallel model in hydrostatic and radiative equilibrium. – The present investigation addresses the question with the example of the Balmer lines in a geometrically simplified one dimensional model of a spherically symmetric expanding atmosphere, employing a state-of-the-art non-LTE radiative transfer code. Despite the simplifications, our model should allow to grasp some essential features. This work can then serve as an exploratory guide to more realistic three-dimensional calculations.

2. Our model

We want to find out, whether the observed splitting of Balmer lines, and their variation as a function of the binary phase is influenced or even determined by scattering and optical depth effects in the outer atmosphere of the red giant. We assume a red giant with given radius, $R_{\rm RG}$, and mass loss, $\dot{M}$.

Send offprint requests to: W. Schmutz

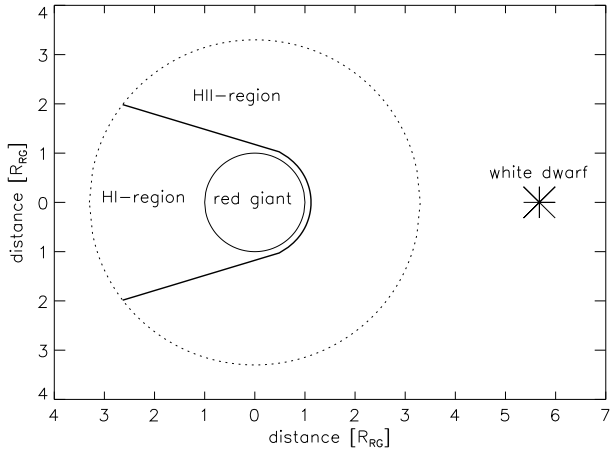

Fig. 1. Ionization front for model 3 (see Table 2) in the atmosphere of a red giant. The front has been calculated with a 2-D nebular model. It places the front at a Strömgren distance, S, from the ionizing radiation source; $S \sim \int n_e^2 ds$.

The atmosphere is composed of hydrogen and a generic metal to account for free electrons due to Mg, Si, and Fe. Its density structure is related to $\dot{M}$ and an assumed velocity law, $v(r)$, that has an inner sub-sonic and an outer supersonic part, with a smooth transition between the two regions. The inner part is formulated to yield a hydrostatic density structure in spherical geometry for the extended atmosphere of the red giant, and the outer part is given by the conservation law of $\dot{M}(r)$ and the usual β-law typical for radiation driven winds (see Hamann & Schmutz 1987).

The red giant is irradiated by the hot white dwarf. It turns out, that in most of our models the actual photosphere of the red giant is not influenced by the irradiation. In a few models with large incident radiation there could be a heating effect by the nebular continuum. However, to facilitate comparisons among the models, we have decided to ignore this effect, and not to modify the temperature structure in the red giant's atmosphere. This results in a reduced flux within the atmosphere, but the emergent continuum flux from the red giant remains identical for all models.

The incident flux and its spectral distribution are defined as coming from a blackbody sphere of given temperature, T_*, and radius, R_*, located at a distance, d, from the center of the red giant. This radiation ionizes a fraction of the wind from the cool star. We calculate the line profiles of the emergent Balmer lines that are created in the ionized and neutral portion of the wind, and determine the location of the emission. We consider only one line of sight. It passes through the white dwarf towards the center of the red giant. This corresponds to the binary phase at maximum light.

We base our calculation of hydrogen line fluxes and profiles on the "Kiel" code for spherically expanding stellar atmospheres (Hamann & Schmutz 1987; Wessolowski et al. 1988). This code has been used extensively to analyze hot stars with strong stellar winds (e.g. Schmutz et al. 1989; Hamann et al. 1991). The

Table 1. Chemical composition of the model atmosphere.

element	abundance	levels
H	99.98 %	H^-, H^+, H^0 (n=1 to n=10)
metal	0.02 %	M^0 , M^+

n = principal quantum number

version employed here is not fully self-consistent, in that we prescribe the density structure by specifying a mass loss rate and a velocity law. The atmosphere calculation then solves for a consistent solution of the non-LTE rate equations and the radiation transfer equations. The line radiation transfer is formulated in the comoving frame. Line broadening is treated as a free parameter, $v_{\rm Dop}$, that is constant throughout the atmosphere.

Beside the parameters specifying the density structure, the model parameters are the effective temperatures of the hot and the cool star, T_* and $T_{\rm eff}$, stellar radii, R_* and $R_{\rm RG}$, and the separation, d, of the stars. Gravity of the red giant is also a model parameter, but this parameter only enters the description of the velocity law at sub-sonic velocities (cf. Hamann & Schmutz 1987). The temperature structure is calculated with a temperature correction method in regions that are optically thick for continuum radiation. In the optically thin part the temperature results from the solution of the energy equation, including cooling by all astrophysically important metals (cf. Schaerer & Schmutz 1994). The non-LTE populations are calculated for a 12-level model atom of hydrogen, with ten levels for neutral hydrogen (n = 1 to n = 10), one level for H^-, and one for H^+. In addition, in order to have a source of free electrons in cool regions of the atmosphere where hydrogen is predominantly neutral, we have a generic metal atom with two ionization stages and an ionization energy of 50 000 $\rm cm^{-1}$. The non-LTE rate equations include bound-bound and bound-free collisions, as well as bound-bound, bound-free, and free-free radiative processes.

Because helium is not included as an opacity source, we restrict the frequency grid to energies below the ionization edge of helium, i.e. we take into account only radiation with wavelengths longer than 504 Å. This is equivalent to the assumption that for shorter wavelengths helium is the dominant, optically thick absorbing agent.

The aim of our work is to investigate the effects of irradiation by a hot source. This problem is inherently non-spherical. However, in order to investigate the basic effects, even a spherically symmetric atmosphere is sufficient to yield significant insight. A spherically symmetric model is almost correct close to the line connecting the two stars. This is due to the combination of density gradient and ionizing radiation. On the irradiated side it places the H^0/H^+ boundary close to the surface of the giant. If this geometry is viewed at maximum light, i.e. when the hot star is in front of the giant, then the observer sees a situation that is nearly identical to a hypothetical front that is concentric around the cool star. We illustrate this point in Fig. 1 which is the result of a 2-D nebular calculation.

3. Method

Our model calculation solves the irradiation problem along the line connecting the two stars. The radiation field is calculated assuming a spherically symmetrical geometry. The asymmetry of the problem increases with the distance from the connecting line. Nevertheless, the physical properties of our model, as a function of distance from the giant, are still a reasonable approximation to all locations that are seen at maximum light. This justifies a comparison of our synthetic line profiles with observations obtained at a phase close to maximum.

3.1. The boundary conditions

Our code is formulated on the basis of discrete radius and frequency grids. To solve the 2nd order differential equations of radiative transfer we iterate on the variable Eddington factor, f, as introduced by Mihalas & Hummer (1974)

$$\frac{d^2\left(f_\nu q_\nu r^2 J_\nu\right)}{dX_\nu^2} = \frac{r^2\left(J_\nu - S_\nu\right)}{q_\nu}\,. \tag{1}$$

The variables have the same meaning as defined in Mihalas (1978). In particular, $dX_\nu = q_\nu d\tau_\nu$.

At the inner boundary we apply a diffusion approximation as formulated by Mihalas & Hummer (1974) to create the radiation field of a red giant with $R_{\rm RG}$ and $T_{\rm eff}$. The inner boundary is located at a Rosseland optical depth of $\tau \approx 10$.

Since irradiation onto a spherically symmetric atmosphere is not described in the literature we present here the formulation of the outer boundary conditions. At the outer boundary, at $R_{\rm max}$, we have a total Eddington flux of

$$H_{\nu,R_{\rm max}} = H^+_{\nu,R_{\rm max}} + H^-_{\nu,R_{\rm max}}\,, \tag{2}$$

where $H^-_{\nu,R_{\rm max}}$ is the contribution from the irradiation by the companion. Analogous to the formulation of the inner boundary condition, we define $h_{\nu,R_{\rm max}} \equiv H^+_{\nu,R_{\rm max}}/J^+_{\nu,R_{\rm max}}$ and we obtain

$$\frac{d\left(f_\nu q_\nu r^2 J_\nu\right)}{d\tau_\nu} = R^2_{\rm max} h_{\nu,R_{\rm max}} J^+_{\nu,R_{\rm max}} + R^2_{\rm max} H^-_{\nu,R_{\rm max}}\,, \tag{3}$$

which is the outer boundary condition to Eq. (1). The outer boundary, $R_{\rm max}$, is chosen as the distance beyond which the essential results do no longer change.

For simplicity we assume the hot radiation source to be an isotropically radiating sphere, i.e. we neglect limb darkening. Thus, the irradiation is given by

$$H^-_{\nu,R_{\rm max}} = \frac{F^{\rm hot}_\nu}{4\pi} \int\limits_{\Omega_{\rm WD}} \cos\theta d\Omega\,. \tag{4}$$

To simplify the model of the hot radiation source, we assume it to radiate as a black-body, i.e. $F^{\rm hot}_\nu = B_\nu(T_*)$.

As a model parameter for our calculations we employ the angle α, which is the white dwarf's half-angle seen from the red giant's surface. This angle is given by $\tan\alpha = R_*/(d - R_{\rm RG})$, where d is the separation of the two stars.

In order to treat the angular dependence of the radiation field, our method requires a ray-by-ray formal solution of the transfer equation for all impact parameters out to $R_{\rm max}$. The rays are placed parallel to the line connecting the two stars, and the atmosphere is only irradiated up to a given impact parameter.

$$I^-\left(z_{\rm max}, p_i, \nu\right) = \begin{cases} B^{\rm hot}_\nu & \text{for } |p_i| \le p_\alpha \\ 0 & \text{for } |p_i| > p_\alpha \end{cases}\,. \tag{5}$$

The limiting impact parameter is given by $p_\alpha = R_{\rm RG}\sin\alpha$. Note that p_α is not the radius of the white dwarf, it is an artificial parameter that is used by the computational scheme to evaluate the angle of the incident radiation (see below). The upper boundary condition of the ray-by-ray formal solution thus reads

$$\left.\frac{du\left(z,p_i,\nu\right)}{d\tau\left(z,p_i,\nu\right)}\right|_{z_{\rm max}} = \begin{cases} \frac{1}{2}\left(I^+\left(z_{\rm max},p_i,\nu\right) + B^{\rm hot}_\nu\right) & \text{for } |p_i| \le p_\alpha \\ 0 & \text{for } |p_i| > p_\alpha \end{cases}\,, \tag{6}$$

with $u = 1/2\left(I^+ + I^-\right)$, and the incident flux for the upper boundary condition of the momentum equation (Eq. 3) is

$$H^-_{\nu,R_{\rm max}} = \frac{B^{\rm hot}_\nu}{4}\sin^2\left(\arcsin\left(\frac{\rm R_{RG}}{\rm R_{max}}\sin\alpha\right)\right)\,. \tag{7}$$

We are aware of the fact, that our computational procedure of the irradiating radiation is not geometrically correct in that it introduces a non-geometrical variation of the incident angle throughout the atmosphere. Since the parameter p_α is constant, for each radius point, r, the angle of irradiation is evaluated as $\tilde{\alpha}(r) = \arcsin(p_\alpha/r)$ (cf. Mihials 1978; Sects. 7-6). This implies a smaller angle of irradiation for points more remote from the red giant and closer to the white dwarf. However, it will turn out, that we deal with a narrow zone of line formation. In this case our treatment only implies a minor systematic modification of the incident luminosity which is not of relevance for the relative comparison of models we are presenting in this work.

3.2. Numerical procedure

We solve the transfer equations with the Feautrier method and iteration for the variables f and h. Consistency with the rate equations is obtained by means of iteration with approximate Λ-operators (Hamann 1985). The irradiation does not change the convergence properties of the atmosphere. However, experience shows that the results are sensitive to how well the ionization front is spatially resolved. It turns out, that the transition between the ionized and neutral part occurs very rapidly. In that transition range several extra radius points are inserted. The front tends to move in the course of the iteration cycles and it is necessary, to follow the front with extra radial points until it is stable.

Because of the smallness of the white dwarf two extra rays had to be added to the grid of impact parameters. They allow to evaluate the small angle under which the white dwarf is seen from the surface of the red giant.

Table 2. Parameters of the calculated models

model No.	1	2	3	4	5	6	7	8	9	10	11	12	13
α [arcmin]	13	13	13	13	1500	23	13	5	3	2	1	0.7	50
$\dot{M}$ [10^{-7}M$_\odot$ yr^{-1}]	0.1	0.2	1	5	0.63	0.63	0.63	0.63	0.63	0.63	0.63	0.63	0.63

α: angle sustained by the radius of the irradiating source as seen from distance $d - R_{\rm RG}$. Parameters common to all models: $T_{\rm RG}$=3500 K, $R_{\rm RG}$=86.4 R$_\odot$, velocity law $v(r) = v_\infty \left(1 - R_{\rm RG}/r\right)^\beta$ with v_∞=100 km s^{-1} and β=1. T_*=100 000K, R_*=0.1 R$_\odot$.

4. The structure of the red giant's outer atmosphere

We apply the above formalism to models with a large range of illuminating angles, but since we only use a limited frequency grid (see Sect. 3), we do not vary the energy distribution of the incident radiation. We assume $T*$ = 100 000 K. Mass loss from red giants is notoriously difficult to determine. For this reason we explore a range of rates, $1 \cdot 10^{-8} \leq \dot{M}[M_\odot/\mathrm{yr.}] \leq 5 \cdot 10^{-7}$ (see Table 2).

In Fig. 2 we show some of the resulting physical characteristics of the irradiated red giant's atmosphere. At the inner boundary the maximum particle density $n_{\rm tot} \approx 6 \cdot 10^{15}$ cm^{-3} corresponds to a Rosseland optical depth of $\tau \approx 6$ in the atmosphere of the M star. The outermost point has $n_{\rm tot} \approx 8 \cdot 10^7$ cm^{-3}, where $n_{\rm tot}$ is the total particle density. The corresponding outer radius is $R_{\rm max}$ = 3.3 R$_{\rm RG}$ = 1.3 AU.

We find a narrow transition zone between the ionized and the neutral part of the atmosphere. Fig. 2c shows that at the ionization front the population of H^0 changes by 5 dex. This is normal for a radiatively ionized nebula, in the case of an irradiated atmosphere the transition can be wider due to optical depth effects. In fact, in the neutral part, the populations do not follow the expectations from nebular theory (see below).

The temperature in the ionized region (Fig. 2a) is of the order of 10 000 K which, again, is typical for H II regions. In the neutral region heating by the incident radiation is negligible and the temperature is determined by the red giant's radiation. As expected, the density where the ionization front occurs, depends on the luminosity of the incident radiation. However, our models yield only a week dependence on the adopted red giant's mass loss. In the case of the example shown in Fig. 2 it coincides with $n_{\rm tot} \approx 10^{11}$cm^{-3}.

Fig. 2d shows the wind velocity as a function of density. (Density and depth are related in Fig. 3a The adopted velocity structure reaches a terminal velocity of 100 km s^{-1} at the outer boundary. This is unrealistically high for a wind from a red giant. However, a comparison with Fig. 2b shows that the line emission has no contribution from the high velocity part. The outer regions have no influence on the model results. Only the low velocity regions and the gradient at the ionization front are of importance for the resulting line profiles. The velocities in the line formation region are of the order of 10 to 30 km s^{-1}, and these values are in agreement with observed mass loss velocities. All models presented here were done for the same velocity law with β = 1 and v_∞ = 100 km s^{-1}.

5. The Balmer decrement

5.1. Observational evidence for non-nebular Balmer decrement

The Balmer decrement in symbiotic stars has been claimed to be different than predicted by the nebular recombination theory. It is difficult to judge the reality of such a statement because the observed line intensity ratios are crucially dependent on the reddening law and the magnitude of the reddening. For a set of 18 symbiotic stars Schulte-Ladbeck (1985) found only marginally significant deviations from case B. However, Blair et al. (1983) report such large discrepancies between the reddening derived from nulling the 2200 Å feature and from the Hα/Hβ ratio, that the assumption of a normal Balmer decrement would imply an extremely unusual UV reddening law. For four systems they derive a significantly larger reddening from the Hα/Hβ ratio. Or, assuming a normal reddening law, this indicates that the intrinsic Hα/Hβ ratio is larger than predicted by recombination theory. In one case, they find a lower reddening, implying a lower Hα/Hβ ratio than case A or B recombination.

In order to study the Balmer decrement we have calculated a series of models with varying ionizing fluxes (Table 2). We find Balmer decrements differing from case A and B recombination theory. In order to understand the reason, we first study the region of line formation before presenting the results.

5.2. The emissivity ratios as a function of location

We define the emissivity ratio, $\Lambda_{\alpha/\beta}$, as

$$\Lambda_{\alpha/\beta} \propto \frac{N_3\, A_{3\,2}\, \beta_{3\,2}\, h\nu_{3\,2}}{N_4\, A_{4\,2}\, \beta_{4\,2}\, h\nu_{4\,2}} \,.$$

$\Lambda_{\gamma/\beta}$ is defined accordingly. N_i represents the population of hydrogen in the quantum state $n = i$, β is the Sobolev escape probability (Castor 1970), and the other symbols have their usual meaning. Note, that we use the Sobolev theory only for the purpose of discussing the results. It is not applied in our numerical calculations. There, the line radiation transfer is calculated in the comoving frame. Nevertheless, the Sobolev theory allows a good insight into the physical processes. We evaluate the Sobolev line optical depths and escape probabilities from the populations of the converged atmosphere model.

The ratios shown in Fig. 4 are based on model 13 of Table 2. They vary in the range $1.4 \lesssim \Lambda_{\alpha/\beta} \lesssim 7$. According to this ratio we differentiate four regimes: (1) At the outer boundary there is a first zone where the line ratio is not far from the nebular theory. (2) In the range of $n_{\rm tot} \approx 10^9$ cm^{-3} we find a zone with enhanced Hα emission. (3) From $n_{\rm tot} \approx 10^9$ cm^{-3} to $n_{\rm tot} \approx 10^{10}$ cm^{-3} there is a sharp transition to a zone of reduced

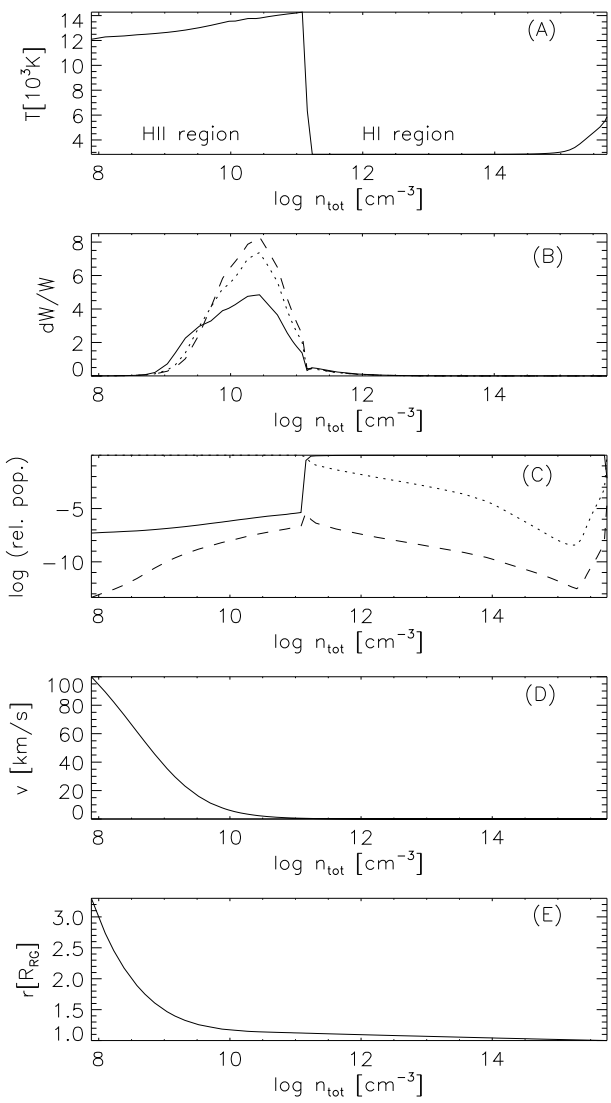

Fig. 2a–e. Physical quantities of model 3 (cf. Table 2) as a function of the particle density, $n_{\rm tot}(r)$. **a** Electron temperature T_e. **b** Fractional contribution dW to the line equivalent widths, W, of Hα (full line), Hβ (dotted), and Hγ (dashed). **c** Relative populations n(HI n=1)$/n_{\rm tot}$ (full line), n(HI n=2)$/n_{\rm tot}$ (dashed), and $\rm H^+/n_{tot}$ (dotted). **d** Velocity v. **e** Radius r corresponding to $n_{\rm tot}(r)$.

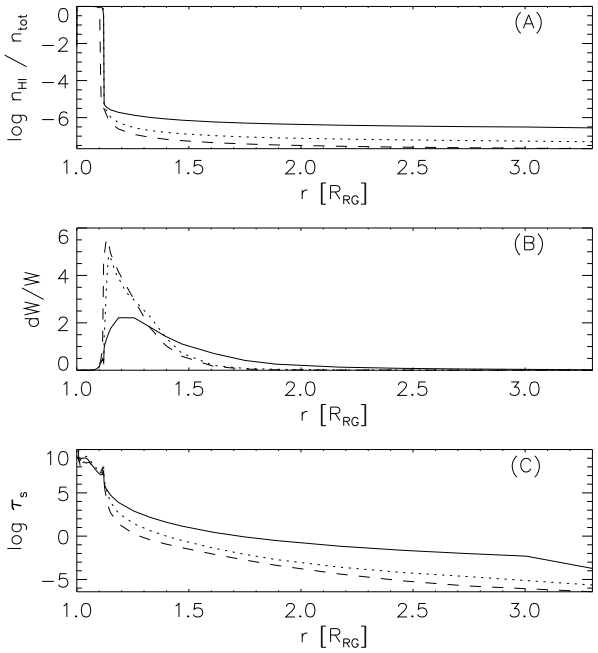

Fig. 3a–c. Physical quantities as a function of radius, r. **a** Relative population of neutral hydrogen. **b** Fractional contribution, dW, from different shells to the equivalent width of Hα. **c** Sobolev optical depth of Hα. The results correspond to three models differing in their mass loss rates: model 2 (- - -), model 3 (. . .), and model 4 (—-).

Hα emission which extends up to $n_{\rm tot} \approx 10^{12}$ cm^{-3}. (4) In the fourth zone, $n_{\rm tot} \gtrsim 10^{12}$ cm^{-3}, hydrogen has recombined. The large variation in the ratios is due to variations in the population processes of the levels n = 3 and 4.

In region (1) we find the Sobolev optical depths of all lines to be much less than one, including the Lyman lines. Our model is an expanding atmosphere, and the low optical depths in the Lyman lines are measured in the direction perpendicular to the expansion direction. Parallel to the expansion, the optical depths of the Lyman lines are of the order of 0.1 which implies, that pumping of excited levels by radiation from the ground state is important. In fact, population of n = 3 and 4 by radiative excitation is larger than population by recombination and subsequent cascading. The radiative transition rates to the ground states differ from the excitation rate. We have therefore neither a case A nor a case B nebula. In contrast to recombination theory, the excited levels are influenced by radiative excitation and we obtain different Balmer emissivity ratios than predicted by recombination theory. For the outermost shell of the atmosphere we find $\Lambda_{\alpha/\beta}$ = 2.33 and $\Lambda_{\gamma/\beta}$ = 0.53. There our model has an electron temperature of T_e = 10,000 K (see Fig. 7. For this temperature case A recombination models yield ratios of 2.86 and 0.47, respectively, and nearly the same values for case B, thus close to our values. We call this the nebular zone.

Due to the spherical expansion of the atmosphere we never encounter a classical case B zone. In region (2) the expansion allows some Lyman photons to escape in directions favored by the expansion and/or acceleration, and the radiative rates of the Lyman lines never cancel each other. At relatively high densities, where expansion velocities become comparable to the adopted turbulence of 10 km s^{-1}, the Lyman lines become optically thick in all directions (see Fig. 5). In the same region also the Balmer lines are close to having a Sobolev optical depth of 1. By inspecting the rates as a function of depth we learn that between the regions of optically thin and thick hydrogen lines there is a zone, where radiative excitation of levels n = 3 and 4 by Lyβ and Lyγ is dominating over population by recombination. Due to the larger optical depth of Lyβ compared to Lyγ (see Fig. 5) the population of n = 3 is favored over n = 4, (see Fig. 6) and the emissivity ratios are in favor of Hα. At $n_{\rm tot} \approx 10^9$ cm^{-3}

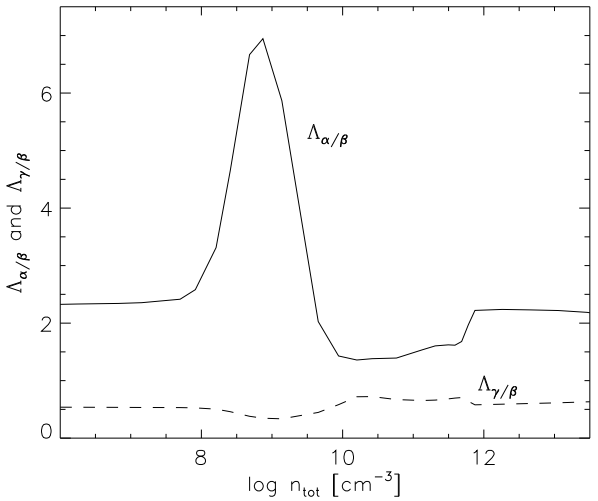

Fig. 4. Emissivity ratios $\Lambda_{\alpha/\beta}$ and $\Lambda_{\gamma/\beta}$ as a function of density for model 13

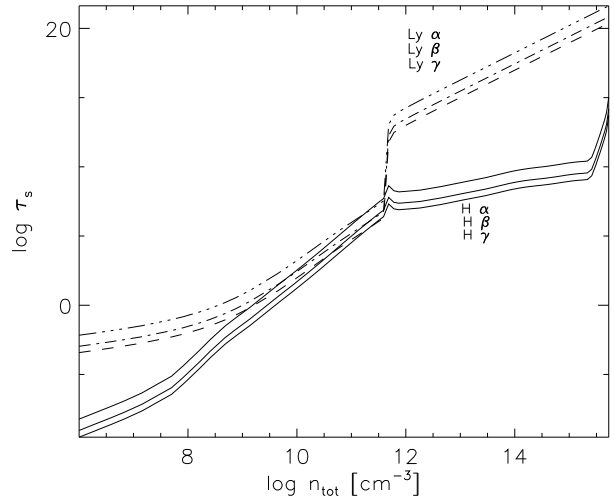

Fig. 5. Sobolev optical depth in direction perpendicular to the expansion direction of Lyα, Lyβ, and Lyγ (dashed lines), and Sobolev optical depth of Hα, Hβ, and Hγ (full lines) as a function of density for Model 13

we find a maximum value of $\Lambda_{\alpha/\beta} \approx 7$, thus, about three times the value expected from recombination theory.

In region (3), where the Lyman and Balmer lines are optically thick the ratio $\Lambda_{\alpha/\beta}$ changes in favor of Hβ. In this region, radiative excitation from $n = 1$ diminishes, and levels $n = 3$ and 4 are predominantly populated by recombination and cascading. But in contrast to the optically thin region, emissivities are strongly influenced by the escape probability of the optically thick Balmer lines. In the example shown in Fig. 4 the emissivity ratio has a minimal value of $\Lambda_{\alpha/\beta} \approx 1.4$. When approaching the recombination front the optical depths of the Balmer lines increase to very large values and the emissivity ratio approaches a value of ≈ 2.2, which is incidently almost the same value as in the nebular zone.

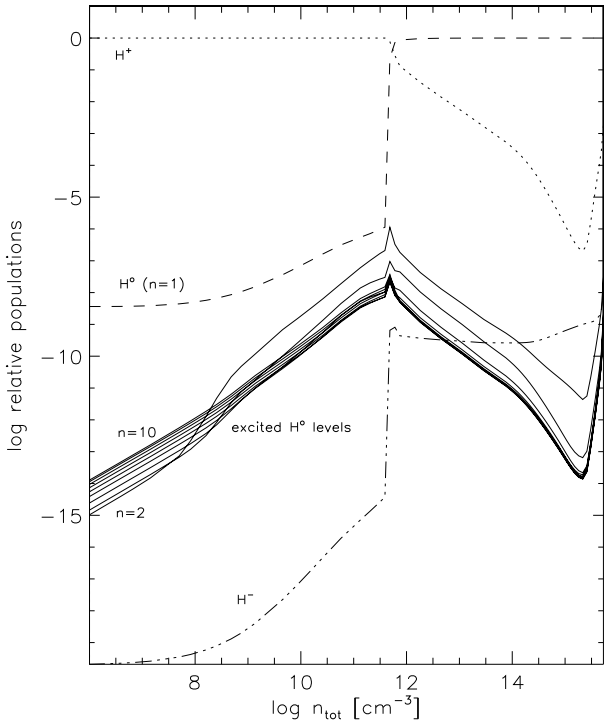

Fig. 6. Relative populations of H^-, H^+, H^0, and the first 9 excited states of neutral hydrogen for Model 13

In the innermost zone (region 4), between the HII region and the stellar surface, where hydrogen is predominantly neutral, our model calculation departs from a nebular situation. Beyond the Strömgren radius of a nebula the excited hydrogen levels and H^+ usually drastically decrease. However, in our irradiated atmosphere populations of excited levels and of H^+ decrease only slowly from the recombination front towards the atmosphere of the red giant. As can be seen from Fig. 6, this is in contrast to the ground state ($n = 1$) in H^0, where the change is abrupt. The reason for this behavior is optical thickness. The photons in a resonance line cannot escape, and therefore the line radiation field sustains the population which in turn leads to an intense line radiation field. The energy that replenishes the inevitable losses comes from ionization and excitation by the radiation field long-ward of the Lyman edge. In this zone ionization of hydrogen depends on populated excited levels, and they in turn, depend on an intense line radiation field.

5.3. The region of line formation

The observed line flux is the result of the integrated light from all zones. Emissivities are weighted by the emitting volume and the escape probability of the photon. Figs. 2b, 3b, and 7 show that the main contribution to the total equivalent width, $W_{\rm tot}$, of the Balmer lines originates close to the $H^+ - H^0$ transition zone. The steep increase of the Sobolev optical depth, i.e. the decrease of the escape probability, shifts the peak contribution to lower densities than prevail in the recombination front. However, in

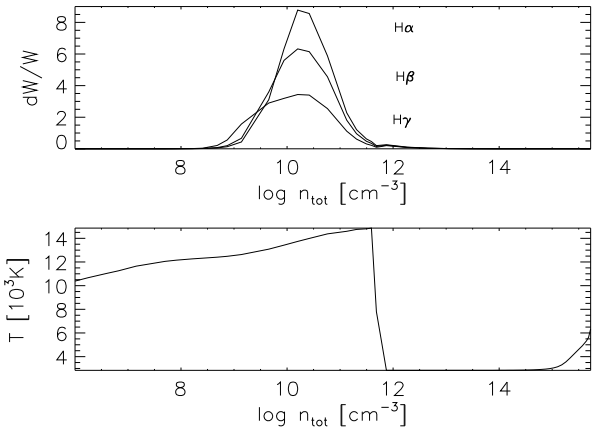

Fig. 7. Upper panel: Relative contributions to the Balmer equivalent widths of Model 13. Lower panel: Electron temperature T_e for model 13 as a function of density.

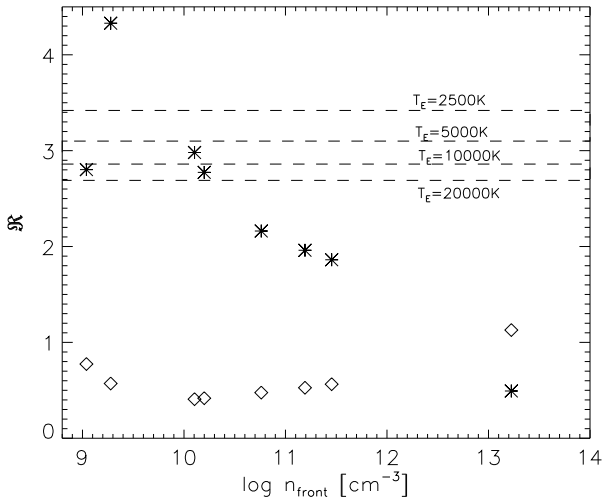

Fig. 8. Balmer decrements, $\Re_{\alpha/\beta}$, for varying ionization fluxes. Dashed lines give case A values of $\Re_{\alpha/\beta}$ for various electron temperatures. Stars stand for $\Re_{\alpha/\beta}$ and diamonds for $\Re_{\gamma/\beta}$ for models 5 (on the right) to 12 (on the left). $n_{\rm rec}$ gives the density, of the corresponding recombination zone.

geometrical units, the main contribution still originates very close to the recombination front.

5.4. The Balmer decrement as a function of mass loss

In order to investigate the effect of the location of the ionization front on the Balmer decrement, we vary the ionizing flux by changing the distance between the two stars. This results in placing the recombination zone at various densities for the different models. The integrated decrement is primarily determined by the location of the recombination front. If the hot object ionizes only the optically thin region, $\Lambda_{\alpha/\beta}$ will be close to the nebular value. It can have different values when the ionization penetrates to deeper layers.

In Fig. 8 we give the Balmer decrements, $\Re_{\alpha/\beta}$, for models 5 to 12 as a function of the density, $n_{\rm rec}$, at the edge of the recombination zone. For comparison we also give the case A values for four different T_e. Our $\Re_{\alpha/\beta}$ vary between 0.49 and 4.33. Most observations of symbiotic systems give values in that range.

6. The line profiles

6.1. Their formation

The complex structure of line profiles from symbiotic systems can give information on different components of the symbiotic system. The information content relative to wind collision zones of forbidden lines has been pioneered by Wallerstein et al. (1984). The Hubble Space Telescope observes profiles that probe the wind of the hot radiation source (Nussbaumer et al. 1995). Absorption lines give access to the photosphere of the cool star. The origin of the Balmer lines is less certain, and its structured emission profiles may be ambiguous, as it is not always clear whether such a profile is a broad emission with absorption components, or consists of several emission shifted features, e.g. the observed line profiles of AG Peg (Boyarchuk et al. 1987), or of RW Hya (Schild et al. 1996).

Fig. 9 shows calculated Hα profiles. If such profiles are observed, it is not at all obvious to the observer whether they are combinations of Gauss profiles, or emission with self absorption, or accretion disk profiles. In our model they are self absorbed emission lines. These line profiles are strongly determined by the velocities in the rather narrow H^0 - H^+ transition region. The asymmetries can be explained in the following way. The blue shifted absorption implies that the absorbing particles approach the observer with higher velocity than those of the underlying recombination zone (P Cygni effect). This is the case because of our velocity law and the spherical symmetry of the expanding wind. The blue shift in the absorption is large if the recombination zone falls into a region with a high velocity gradient dv/dr. Their asymmetry increases with increasing $\dot{M}$. An increase in the mass loss implies an outward shift of the recombination zone. In models 3 and 4, with $\dot{M} \geq 10^{-7}$M$_\odot$/yr, the gradient within the recombination zone is particularly steep. In models 1 and 2 the recombination zone lies deeper in the atmosphere, and the velocity is nearly constant, emission and absorption originate from regions with similar line of sight velocities. This leads to a symmetrical line profile.

Fig. 10 shows Hα profiles obtained from models 5 to 12. They have been normalized to the same peak value. The asymmetry of the increases with increasing stellar separation which corresponds to decreasing incident flux. Decreasing flux shifts the recombination zone to smaller densities and larger r, where the velocity gradient is larger.

We also see that the equivalent widths, W, are not on a monotonous slope. W is determined by (a) the incident flux, (b) by the absorbing column density which depends on the density-location of the H^0 - H^+ transition region, and (c) by the contin-

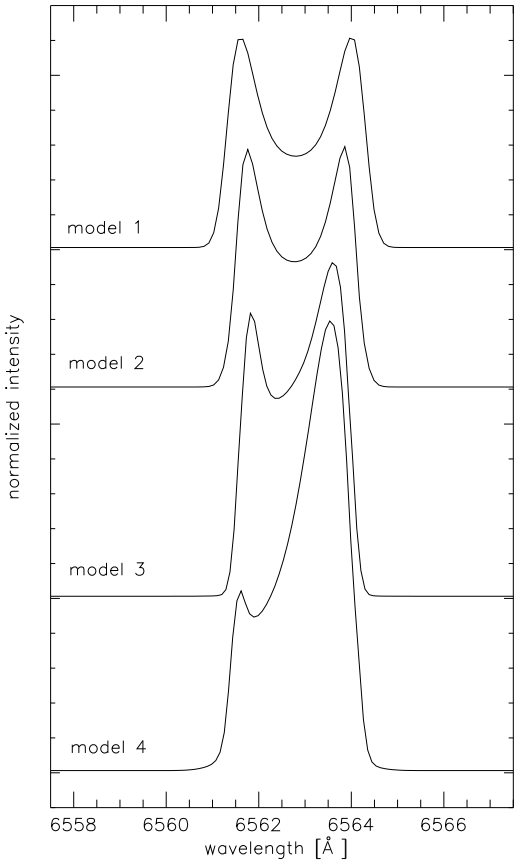

Fig. 9. Hα profiles calculated for different $\dot{M}$.

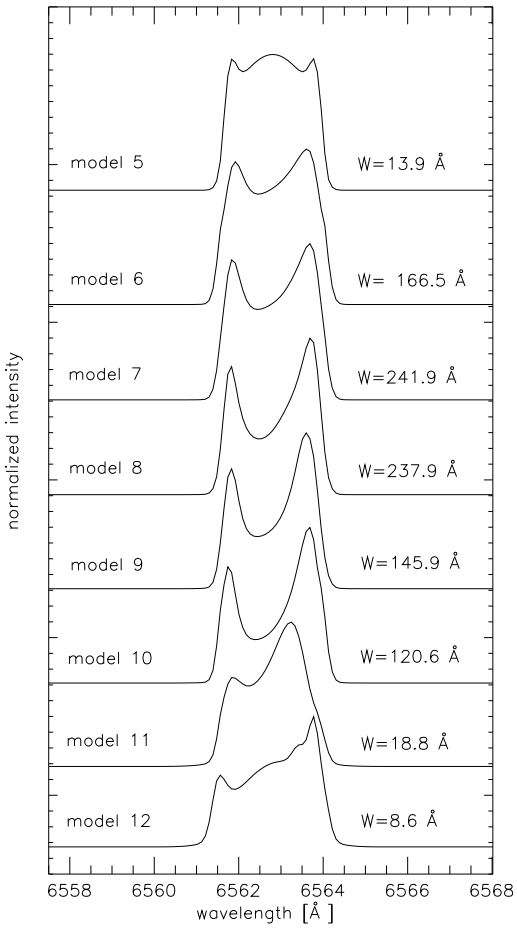

Fig. 10. Normalized Hα- lines for models 5 to 12.

uum flux level which is enhanced by the nebular contribution originating in the H II region of the wind. Fig. 11 shows the luminosities for the Hα- and Hβ- lines for models 5 to 12. The line luminosities increases with increasing $n_{\rm rec}$, as this implies increasing irradiation due to decreasing distance of the irradiating source (higher α). Model 5 has a particularly high α (see Table 2) and thus, the largest incident luminosity.

6.2. Comparison with observed line profiles

We now apply our model to SY Mus. Models 3 and 7 yield profiles that closely resemble that of SY Mus at phase 0.52 (Schmutz et al. 1994), i.e. close to maximum light. This corresponds approximately to our model assumption, where the hot star lies on the line of sight to the red giant. In Fig. 12 we compare the normalized Hα profile of model 3 with the observation. The observed profile was shifted by 0.28Å to the blue in order to account for the system velocity of $v_{\rm sys}$ = 13 km s^{-1}. Fig. 12 demonstrates that the profile predicted by the model reproduces well the central part of the observed profile of an S-type symbiotic. This supports the validity of our model assumptions for the formation of Balmer lines.

The strength of the calculated profile relative to the continuum is about twice that of the observed profile. This difference is not surprising given the parameters of model 3. SY Mus contains a white dwarf of $T*$ = 100 000 K and $R*$ = 0.1 R$_\odot$ (Mürset et al. 1991) at a distance of 1.33 AU irradiating the surface of a red giant with $R_{\rm RG}$ = 86.4 R$_\odot$ (Schmutz et al. 1994). The illumination angle of SY Mus is therefore α = 1.4 arcmin. Thus, the illumination angle of model 3 is too large, which implies an incident luminosity that is too large, the calculated lines will therefore be too strong. On the other hand, models 10 and 11, that are closest to the correct illumination angle, predict lines that are slightly too weak, and profiles that fit less well than model 3. From our results of Sect. 5.4 we expect an improvement in the profile by adjusting the mass loss rate. However, a perfect fit will not be possible since the line strength depends mainly on the incident luminosity and varies only little for different mass loss rates.

The Balmer lines are formed where the wind is accelerated from subsonic to $\approx$ 20 km s^{-1} with the main emission from regions with expansion velocities of 10 km s^{-1} or less. To reproduce the width of the profile we had to assume a broadening of 19 km s^{-1}. The electron temperature at the ionization edge is T_e = 13 000 K, and temperature broadening accounts for $\approx$ 15 km s^{-1}. As we have not accounted for the splitting of Hα into $\lambda\lambda$6562.74, 6562.81, 6562.86, our result implies that

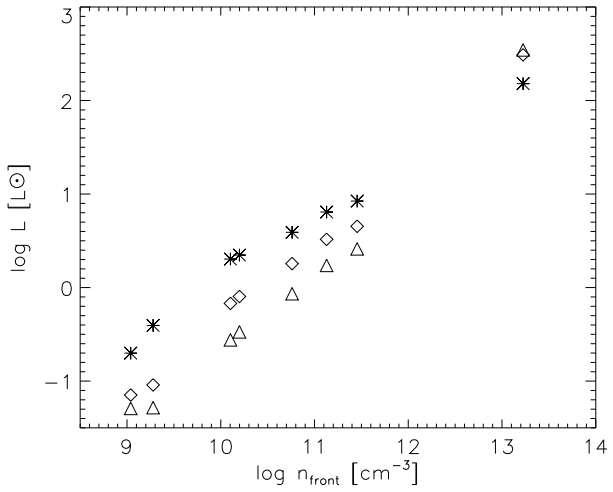

Fig. 11. Luminosity in Hα (*), Hβ (squares), and Hγ (triangles) as a function of $n_{\rm tot}$, as found in the recombination zone for models 5 to 12. Model 5 is on the right, then follow from right to left, models 6 to 12.

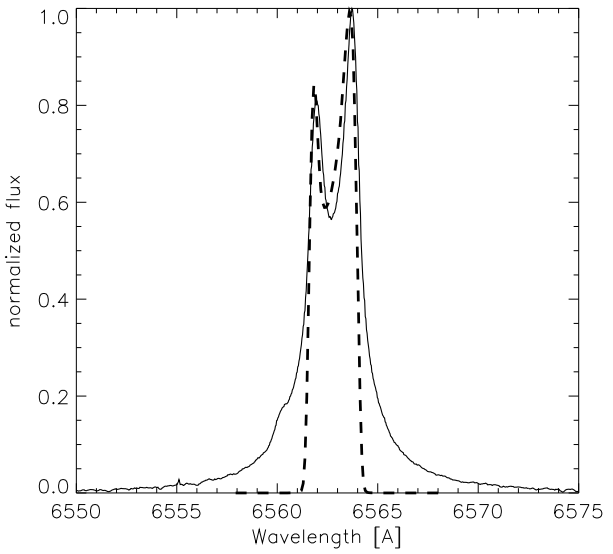

Fig. 12. Normalized observed Hα profile of SY Mus for phase 0.52 (full drawn line) compared to the calculated normalized profile of model 3 (dashed).

there is none or only little additional broadening due to turbulent motion.

In the models investigated, the widths of the profiles depend only on broadening and not on the expansion of the red giant's wind. We have assumed a wind velocity law that accelerates up to 100 km s^{-1}. Such a law is not expected for a red giant. However, the observed Balmer profile of SY Mus (see Fig. 12) and of many other symbiotic stars have a broad line wing. The main reason for adopting such a velocity law was the idea that the line wings are formed in a fast expanding red giant wind. Our calculations demonstrate that the line wings are of a different origin. Although our models include larger expansion velocities the synthetic profiles do not reflect them. The emergent profile is determined by a narrow formation region where the wind expansion is slow, and the densities are high.

7. Conclusions

What do profiles of the Balmer lines tell us about the nebular environment in symbiotic systems? We model the system as a binary composed of a mass losing red giant, and a black body companion as source of the radiation that ionizes the wind of the giant. We chose a line of sight through the ionizing source in direction of the mass losing star. In our model the particle density decreases with increasing distance from the giant.

We find that the observed Balmer emission lines are predominantly formed close to the recombination zone which separates the H^0 from the H^+ region. This is easy to understand. Balmer emission is mainly due to recombination which grows as $n_{\rm H^+} \cdot n_{\rm e}$. The recombination boundary is the location of highest density within the H^+ region. Within the neutral region optical depth becomes prohibitive with increasing distance from the recombination boundary. If ionization is restricted to the low density nebular part of the wind, the relative strengths of the Balmer lines are close to the nebular case A. That is different if ionization penetrates to higher densities. The resulting value then depends on the detailed population mechanism of the individual states. It is important to see, that even at high radial optical depth case B may not occur because photons can escape at right angles to the wind direction.

When illuminating a stellar atmosphere from the outside, the radiation meets a fast increasing density. The line emission increases with the square of the density, and the integral of the emission is heavily weighted by a narrow, dense region located at the boundary of the Strömgren sphere. Line profiles strongly depend on the velocity gradient of the expanding wind close to that recombination boundary. Whereas observed profiles might suggest two gas streams, or wind components of possibly similar velocities in different directions, our model calculations show that self absorption within an accelerating wind might be a more natural explanation.

Acknowledgements. We thank our colleagues from the Institute of Astronomy for fruitful discussions.

References

Blair W.P., Stencel R.E., Feibelman W.A., Michalitsianos A.G., 1983, ApJS 53, 573
Boyarchuk A.A., Belyakina T.S., Tarasov A.E., Glagolevski Y.V., 1987, Ap&SS 131, 775
Castor J.I., 1970, MNRAS 149, 111
Dobrzycka D., Kenyon S.J., Mikolajewska J., 1993, AJ 106, 284
Hamann W.-R., 1985. In: Numerical radiative transfer, ed. Kalkofen W., Cambridge University press, Cambridge, p. 35
Hamann W.-R., Schmutz, W. 1987, A&A 174, 173
Hamann W.-R., Dünnebeil G., Koesterke L., Schmutz W., Wessolowski U., 1991, A&A 249, 443
Ivison R.J., Bode M.F., Meaburn J., 1994, A&AS 103, 201
Kenyon S.J., Mikolajewska J., 1993, Mikolajewski M., Polidan R.S., Slovak M.H., 1993, AJ 106, 1573

Mihalas D., 1978. Stellar Atmospheres, 2nd Ed., Freeman and Company, San Francisco.
Mihalas D., Hummer D.G., 1974, ApJS 28, 343
Mürset U., Nussbaumer H., Schmid H.M., Vogel M., 1991, A&A, 248, 458
Nussbaumer H., Schild H., Schmid H.M., Vogel M., 1988, A&A 198, 179
Nussbaumer H., Schmutz W., Vogel M., 1995, A&A 293, L13
Proga D., Kenyon S.J., Raymond J.C., Mikolajewska J., 1996, ApJ 471, 930
Schaerer D., Schmutz W., 1994, A&A, 288, 231
Schild H., Mürset U., Schmutz W., 1996, A&A 306, 477
Schmutz W., Hamann W.-R., Wessolowski U., 1989, A&A 210, 236
Schmutz W., Schild H., Mürset U., Schmid H.M., 1994, A&A 288, 819
Schulte-Ladbeck R.E., 1985, PhD Thesis Univ. Heidelberg
van Winkel H., Duerbeck H.W., Schwarz H., 1993, A&AS 102, 401
Wallerstein G., Willson L.A., Salzer J., Brugel E., 1984, A&A 133, 137
Wessolowski U., Schmutz W., Hamann W.-R., 1988, A&A 194, 160

This article was processed by the author using Springer-Verlag LaTeX A&A style file *L-AA* version 3.